Observation of magnetic resonance of electron spins with engineered membrane resonators

by

Dylan Patrick McNally

A thesis submitted to the

Faculty of the Honors Council of the

University of Colorado at Boulder in partial fulfillment

of the requirements for the degree of

Bachelors of Science with Honors Distinction

Department of Physics

2019

This thesis entitled:
Observation of magnetic resonance of electron spins with engineered membrane resonators
written by Dylan Patrick McNally
has been approved for the Department of Physics

Professor Cindy A. Regal
Advisor, Department of Physics

Professor Jun Ye
Honors Council Representative, Department of Physics

Professor Yung Chen Lee
Department of Mechanical Engineering

Date _____

The final copy of this thesis has been examined by the signatories, and we find that both the content and the form meet acceptable presentation standards of scholarly work in the above mentioned discipline.

McNally, Dylan Patrick (B.S., Engineering Physics)

Observation of magnetic resonance of electron spins with engineered membrane resonators

Thesis directed by Professor Cindy A. Regal

Advisor, Department of Physics

Within the field of nuclear magnetic resonance (NMR), it has long been considered that using force-based detection instead of a pick-up coil for electromagnetic waves may be an intriguing way to achieve nanoscale resolution for detection of nuclear spins. This idea, known as magnetic resonance force microscopy (MRFM), is nonetheless a very difficult experimental proposition due to the extremem sensitivities necessary. Silicon nitride membrane resonators are one potential way that we want to explore increasing the force sensitivity of MRFM devices and improving imaging resolution. Specifically, engineered silicon nitride resonators may have lower surface noise effects due to higher frequencies and reduced force noise floors do to high quality factors. In my thesis, we took a first step towards this goal, demonstrating observation of magnetic resonance of electron spins in DPPH (a spin sample that is easier to detect both in concentration and gyromagnetic ratio) and achieve force sensitivities as low as 67 aN/$\sqrt{\text{Hz}}$. Additonally, future membrane resonators are introduced that hint at force sensitivities as low as 0.6 aN/$\sqrt{\text{Hz}}$ with resonant frequencies above 1 MHz. Finally, discussion is opened around the integration of MRFM devices into an optical cavity, for which silicon nitride membrane resonators as used in the Regal group are aptly fit. Benefits of cavity optomechanical integration lie in passive damping of the mechanics to increase measurement bandwidth and improved detection sensitivity.

Dedication

To my parents, who gave me every opportunity I could want and shaped the person I am. To my brother and sister for their eternal love and friendship.

Acknowledgements

My undergraduate research began with the Lee Group in Mechanical Engineering. Without this experience and the guidance of Y.C., Ryan, Shanshan, Alex, and Collin I would not have many of the valuable skills that made my current research possible. Thank you.

The work here-in presented would not have been possible without the minds and support of countless people. The Regal Group, especially Ran, Chris, Gabriel, Tom, Max, Pete and Ben, were instrumental in helping me solve problems, fixing my mistakes, and making the lab a spectacular working environment. Gabriel is the principle mastermind behind the design of the mechanics discussed and used, especially in section 4.3. Chris and I worked side-by-side in the lab and helped me understanding difficult physics just a little bit better. Ran was an incredible mentor and is largely responsible for the design of our devices. Thank you all.

Finally, this work would not be possible without the support and faith of Cindy. I am grateful to her for the opportunity to be apart of such a brilliant group of scientists. My time in the Regal Group is the undoubtedly the highlight of my undergraduate education. Cindy believed in me and my capacity as a student and researcher, even when I did not and has gone above and beyond for me as an advisor on multiple occasions. Thank you.

Contents

Chapter

Tables

Table

Figures

Figure

Chapter 1

Introduction

In 1922 Otto Stern and Walther Gerlach discovered the quantum nature of electron spins. By passing a beam of silver atoms through a magnetic field, they observed that the displacement of the atoms due to magnetic force was quantized. This insight suggests that the orientation of the angular momentum about an elementary particle's axis is quantized. The quantization of the spin angular momentum comes with associated energy levels and eigen-states when the spin is interacting with external fields. For example, when in a strong magnetic field, the spin will align with the lowest energy eigen-state.

Magnetic Resonance is an interesting phenomena that occurs when the spin is then perturbed from this low-energy state. Commonly done with a weaker magnetic field, this perturbation will cause the spin to precess at a frequency defined by the strength of the magnetic field and the particular particle. This resonance emits electromagnetic radiation that can be detected with a coil or even by measuring magnetic force interactions, as is demonstrated in this thesis in a technique known as Magnetic Resonanc Force Microscopy (MRFM).

Longstanding interest in measuring small forces has driven development of more precise measuring techniques and devices. Optical interferometry is a valuable tool for measuring position of objects to a high degree of precision. One salient example of the use of interferometry is the detection of gravitational waves by the LIGO experiment, where the motion of kg scale mirrors was observed. As mentioned above, spins (even nuclear spins, NMR) can be detected by measuring magnetic forces from the spin magnetic moments. However, measuring this force requires advanced

techniques and devices because it is a very small force. Interferometry can be used to measure the motion of a mechanical resonator acted on by this force, but the methods of interferometry and the mechanical resonator used affect the sensitivity of the device.

1.1 Magnetic Resonance Force Microscopy

Magnetic Resonance Force Microscopy (MRFM) is a niche field of study within NMR and MRI. MRFM combines the techniques of magnetic resonance imaging (MRI) and scanning microscopy. Instead of using a pick-up coil to detect the electromagnetic signal from the resonant spins, MRFM measures the force of the magnetization of a sample interacting with a nearby permanent magnet. The magnetic dipole of electron or nuclear spins interacts with a high magnetic gradient to drive a resonator. The behavior of this resonator is then observed to calculate the magnetic force and then measure the magnetization of the sample. MRFM is a desired imaging technique because it reduces the number of spins required for imaging and thus increases the resolution of imaging. Single-spin detection could lead to full 3-dimension imaging of proteins, bacteria, and other microscopic subjects with atomic resolution [4, 5, 6].

MRFM has been demonstrated with optically observed micro-mechanical resonators including cantilevers [7] and tensioned membrane resonators [8]. While it has been demonstrated that MRFM can reach nm scale resolution and attonewton scale force detection [9, 10], employing more advanced mechanical resonators and device geometries could push force noise floors to sub-attonewton levels [11, 12, 13, 14]. Additionally, engineered mechanical membrane resonators have higher frequency modes than previously used resonators. Surface noise effects are a large problem withing MRFM; this noise scales as $1/f$ so the higher frequency membrane resonators have potential promise in reducing the noise, allowing for closer positioning of the mechanics to the surface. The Regal group also recognizes the potential for direct resonant coupling to spins at the 10 MHz level and above. Yet, all of these possibilities are hypotheses to date in devleopment of this project, and my goal was to develop tools to observe a first spin signal with an engineered membrane resonator.

1.2 Problem Statement

This thesis describes a demonstration of MRFM with a silicon nitride (Si_3N_4) tensioned, membrane resonator. The goal of the experiment, and this thesis, is to demonstrate magnetic resonance force detection of electron spins in a test sample using a functionalized Si_3N_4resonator. This proof of concept opens up discussion of steps to use a variety of developments in mechanical resonators and their optical detection that have been developed in the Regal group, and other groups around the world, in the field of cavity optomechanics to potentially make progress towards long sought goals in the difficult task of MRFM with nuclear spins.

The work presented within is the culmination of efforts from many smarter minds than myself. I am fortunate enough to have been apart of such an experiment. My main contributions to the experiment, which this thesis will dive into, come in making the ideas a reality. Fabrication of the presented devices is a difficult, precise task that was my main charge. I worked closely with Chris in fabricating the engineered membrane resonators, especially the phononic crystal structures, and Ran in fabricating the complete MRFM device. As I built the devices, it mandated a knowledge of why I was building this device and why it was designed as it was. Following the successful fabrication of the device came the experimentation and characterization of the magnetic force sensing. Gabriel and I worked together in measuring the mechanical properties of the engineered membrane resonators and measuring the magnetic forces and data taking. As with the fabrication, this mandated learning what I was measuring and why I was measuring it. Presented in this work are the skills, knowledge, and experiences gained in answering the question: how does one sense electron spin realizations using a type of resonator that the Regal group works with, referred to as engineered membrane resonators.

1.3 Thesis Organization

This dissertation aims to open up a discussion surrounding MRFM. Ch. 2 reviews the field of cavity optomechanics, focusing on notable past achievements and the basic science of interacting

electromagnetic radiation and mircomechanical and nanomechanical resonators. Ch. 3 dives into the physics surrounding spin modulation and the drive of the magnetic dipole moments. Following understanding of the drive of the spins, Ch. 4 covers the method of detection - resonator mechanics, including design, fabrication, measurement, and exploration of future, more elaborate devices. Ch. 5 brings these two elements together and discusses the design and geometry of the MRFM device. Finally, I will conclude with a discussion of results and a brief consideration of the path forward for further research.

Chapter 2

Optomechanics

2.1 Introduction

In 1619, Johannes Kepler published *De Cometis Libelli Tres* with his observations of the behavior of comets. In *De Cometis*, Kepler observed that a comet's tail always pointed away from the sun, and thus postulated that light carries momentum. The radiation pressure force of electromagnetic waves has more recently been studied in the twentieth and twenty-first centuries.

This radiation pressure force can interact with macroscopic objects, acting on a mechanical resonator, or being acted on by said resonator. The force can also be used to trap or suspend particles in a focused laser beam [15]. This effect can be used to cool atomic motion and reduce a system to its ground state.

2.2 Optical Interferometry

An interferometer is a useful tool for scientists to measure the position of an object with respect to another by the interference property of light. In MRFM, an interferometer is used to detect the motion of the force sensing resonator. Similarly, our experiment uses a Michelson interferometer to observe the motion of the cantilever. A Michelson interferometer has monochromatic light that is split by a beam splitter into two perpendicular beam paths. Each path is retroreflected incidently onto the beam splitter and the two beams are combined, mathematically explained by the superposition of the electromagnetic waves. While the waves will have the same phase when they are first split, they will acquire different phases based on the length of each arm of the interfer-

ometer. This phase difference will lead to constructive or destructive interference. The combined beam is then directed towards some photodetector that analyzes the signal.

If one of the path lengths is changing with respect to the length of the other arm of the interferometer, then the interference, and thus the intensity of the light will vary with time. Analysis of the spectrum of the light yields information about the relative positions of the two mirrors. For example, if one of the mirrors is a reflective micromechanical resonator, the modes of the resonator will be seen in the power spectral density.

2.3 Cavity Optomechanics

Now we introduce a situation in which light is reflected back and forth many times between two mirrors as seen in Fig. 2.1.b. This build up of power within the cavity can give rise to nonnegligible radiation pressure forces needed for optical damping and more sensitive detection.

The most basic optical resonator is a Fabry-Pérot cavity, as seen in Fig. 2.1.b. Two parallel mirrors form an optical cavity. Due to the interference of electromagnetic waves, only certain modes of light exist within the cavity, whose wavelength and frequency are determined based on the length of the optical cavity. The allowed frequencies are given by the relation:

$$\omega_{cav,m} = \frac{m\pi c}{L} \tag{2.1}$$

These transverse modes differ in frequency space by a quantity called the Free Spectral Range (FSR), equal to mc/L. For simplicity, one transverse mode is considered, labeled ω_{cav}. When monochromatic light of frequency ω_L is input into one end of the cavity, the radiation pressure then causes the movable mirror at the other end to oscillate. The interaction with the mechanical object introduces a laser detuning of:

$$\Delta = \omega_L - \omega_{cav} \tag{2.2}$$

The frequency shift describes how the laser frequency is either closer to or farther from the

cavity resonance. This will change the intensity or amount light that is inside the cavity. This is equivalent to the difference between the pump tone frequency and the cavity frequency. When these differ in frequency by the mechanical frequency, as seen in Fig. 2.1.c, then a photon from the pump light and a phonon from the mechanics combine to create a phonon at the cavity resonance. A more detailed discussion of this phenomenon can be found in [16, 17]. As the resonator gives up phonons, it is damped or cooled by the loss of acoustic energy. This effect increases the linewidth of the mechanical resonance without changing frequency significantly.

Radiation pressure cooling is not the only method of cooling; in fact active damping is a very common technique in a variety of sensors, including MRFM devices. There are advantages to passive damping so the discussion of other methods and coupling regimes is left to [16, 17].

2.4 Applications of Mechanical Damping

Optomechancial damping has been used to cool resonators down to near the quantum ground state using radiation pressure cooling[18, 19, 20, 21, 22, 23]. Optomechanical damping of the mechanical resonator is beneficial to the experiment described in the following chapters as it increases stability of the resonance and the bandwidth at which measurements can be made of the mechanical object. While this does not directly benefit the force sensitivity of the resonator used, the increase in bandwidth is preferred. While the following experiment is not to date integrated in an optomechanical cavity, demonstrating detection of electron spins with the advanced membrane-type mechanical resonators is the first step to achieving this. This serves as motivation for the discussed experimental design as Si_3N_4membrane resonators are aptly fit for cavity optomechanics uses.

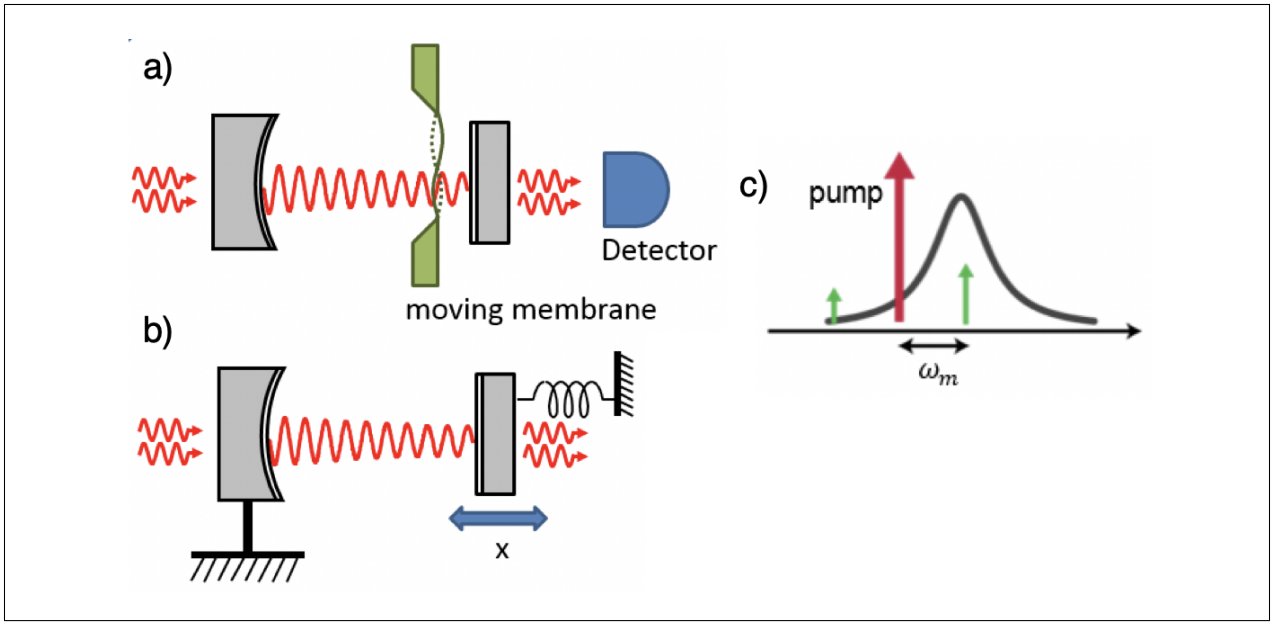

Figure 2.1: a) Membrane-in-the-middle optomechanical cavity. b) Fabry-Pérot cavity with one fixed and one movable mirror. c) Spectrum of optomechanical coupling in the resolved sideband regime.

Chapter 3

Electron Ensemble Spin Mechanics

3.1 Introduction

An electron orbiting a nucleus has two forms of angular momentum. The first is orbital angular momentum that interacts with energy levels. The second is spin, the angular momentum of the electron spinning much like the Earth rotates about its own axis. Because the electron is a charged particle, the spin of the electron introduces a magnetic moment in the electron. This magnetic moment can be measured by sending particles through an external magnetic field and observing the trajectory. This experiment, known as the Stern-Gerlach experiment, first demonstrated the quantum nature of spin by finding that there were only two trajectories that correlated to an up and a down spin.

3.2 Quantum States of Electron Spins

The behavior of an electron spin is described by the Schrödinger equation

$$i\hbar|\psi(t)\rangle = H(t)|\psi(t)\rangle \tag{3.1}$$

The solution to the Schrödinger equation with a time-independent Hamiltonian is given by

$$|\psi(t)\rangle = \sum_n c_n e^{-iE_n t/\hbar}|E_n\rangle \tag{3.2}$$

The probability of measuring each energy level, $P(E_n) = |c_n|^2$, is time-independent. However, if a perturbation, for example an observable that does not commute with the Hamiltonian, is introduced, then the new eigenstates would be a superposition of the Hamiltonian eigenstates and the probabilities would become time dependent. The time dependence is given by the Bohr frequency, which is the difference between energy levels divided by $\hbar$.

With a spin-1/2 system such as the electron, the Hamiltonian is given by the negative of the dot product of the magnetic dipole from spin and the external magnetic field. In a uniform magnetic field along $\hat{\mathbf{x}}$, this is simplified as:

$$H = -\mu \cdot \mathbf{B_0} = \omega_0 S_x \tag{3.3}$$

Here we define $\omega_0 = \gamma B_0$ as the Larmor Frequency and will set the angular frequency of spin precession. The two energy levels are $\pm\hbar\omega_0/2$, seperated by an energy difference of $\hbar\omega_0$. If we consider any general, time dependent superposition state

$$|\psi(t)\rangle = \begin{pmatrix} e^{-iE_+ t/\hbar}\cos(\theta/2) \\ e^{-iE_- t/\hbar}e^{i\phi}\sin(\theta/2) \end{pmatrix} \tag{3.4}$$

$$= e^{-i\omega_0 t/2}\begin{pmatrix} \cos(\theta/2) \\ e^{i(\phi+\omega_0 t)}\sin(\theta/2) \end{pmatrix} \tag{3.5}$$

While the expectation value $\langle S_x \rangle$ is constant in time ($\hbar\cos(\theta)/2$), the perpendicular spin components are not. The time-dependent expectation values are included below and visualized in Fig. 3.1.

$$\langle S_z \rangle = \frac{\hbar}{2}\sin\theta\sin(\phi + \omega_0 \mathrm{t}) \tag{3.6}$$

$$\langle S_y \rangle = \frac{\hbar}{2}\sin\theta\cos(\phi + \omega_0 \mathrm{t}) \tag{3.7}$$

The expectation values of spin are then reduced to classical descriptions that rotate at the

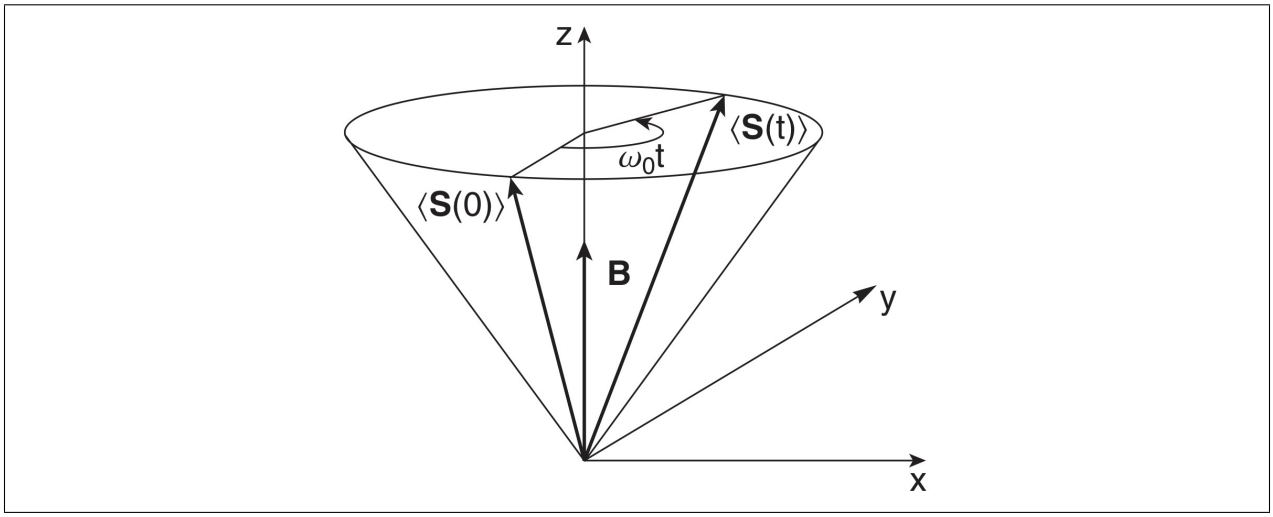

Figure 3.1: Expectation value of spin in precession. Note McIntyre has the external magnetic field in the $\hat{\mathbf{z}}$. I use $\hat{\mathbf{x}}$ for translation to MRFM and membrane mechanics. From [2]

Larmor frequency, ω_0. The precession can be treated as classical dynamics. The equation of motion of the angular momentum is given by the torque of a magnetic moment in a uniform magnetic field.

$$\frac{d\boldsymbol{\mu}}{dt} = \gamma \boldsymbol{\mu} \times \boldsymbol{B} \tag{3.8}$$

The sample overall magnetization has the same behavior as the individual moments described in Eq. 3.8. Further, Ehrenfests Theorem allows us to treat the expectation values of the spin components classically.

3.3 Precession in a General Direction

The above section considers the behavior of a single spin in a uniform magnetic field in the $\hat{\boldsymbol{x}}$ direction. To understand the driving of spins in magnetic resonance, a magnetic field in a general direction is considered. To start, we maintain the initial field $B_0\hat{\boldsymbol{x}}$ and add a smaller field in a perpendicular direction

$$\boldsymbol{B} = B_0\hat{\boldsymbol{x}} + B_1\hat{\boldsymbol{z}} \tag{3.9}$$

The field can be treated as a superposition of two fields. Then decomposing the components, we get two Larmor Frequencies $\omega_0 = \gamma B_0, \omega_1 = \gamma B_1$.

The resulting Hamiltonian is simply:

$$H = \frac{\hbar}{2}\begin{pmatrix} \omega_0 & \omega_1 \\ \omega_1 & -\omega_0 \end{pmatrix} \tag{3.10}$$

This can be similarly written in the $\hat{\boldsymbol{n}}$ basis along the direction of the resulting magnetic field direction. Applying a rotation matrix with angle θ defined as that between $\boldsymbol{B}$ and $\hat{\boldsymbol{x}}$. Considering this rotation, we can write the eigen-states of the spin in the $\hat{\boldsymbol{n}}$ basis as a superposition of spin up and spin down states in the $\hat{\boldsymbol{x}}$ direction.

$$|+\rangle_n = \cos\frac{\theta}{2}|+\rangle + \sin\frac{\theta}{2}|-\rangle \tag{3.11}$$

$$|-\rangle_n = \sin\frac{\theta}{2}|+\rangle - \cos\frac{\theta}{2}|-\rangle \tag{3.12}$$

To take a step back, our goal is to use magnetic resonance to cause a spin to flip back and forth in a manner that we can detect using magnetic force interactions with a nearby resonator. So then it follows that we consider a spin starting in the $|+\rangle$ state in the $\hat{\boldsymbol{x}}$ direction and derive the probability of observing it in the $|-\rangle$ state in the $\hat{\boldsymbol{x}}$ direction. Take then a spin starting in the spin up state in the $\hat{\boldsymbol{x}}$ direction written in the $\hat{\boldsymbol{n}}$ basis and consider it over time as in Eq. 3.2.

$$|\psi(t)\rangle = e^{-iE_+t/\hbar}\cos\frac{\theta}{2}|+\rangle_{\mathrm{n}} + \mathrm{e}^{-\mathrm{iE}_-\mathrm{t}/\hbar}\sin\frac{\theta}{2}|-\rangle_{\mathrm{n}} \tag{3.13}$$

The time dependence is described by the energy levels $E_\pm$ found by solving for the eigenvalues of Eq. 3.10. The probability of the spin flip is then given by Rabi's formula:

$$P_{+\to-} = |\langle-|\psi(t)\rangle|^2 = \frac{\omega_1^2}{\omega_0^2+\omega_1^2}\sin^2\left(\frac{\sqrt{\omega_0^2+\omega_1^2}}{2}\mathrm{t}\right) \tag{3.14}$$

However, for this probability to be of any significance our secondary magnetic field needs to be very large compared to B_0. To avoid this, we consider a time dependent magnetic field with frequency at or near the Larmor frequency set by B_0. In doing so, a change of coordinates to a rotating frame at the Larmor frequency allows a simplification of the precession and the ability to drive spin flips with perturbation fields of small magnitude.

3.4 The Rotating Wave Approximation

To make the spins flip without applying a large perturbation field, a time dependence with frequency ω is introduced instead of a constant field. This rotating field takes the form of

$$B_{rot} = B_1(\cos(\omega\mathrm{t})\hat{\mathbf{z}} + \sin(\omega\mathrm{t})\hat{\mathbf{y}}) \tag{3.15}$$

Then, with the uniform magnetic field introduced in Sect. 3.2, $\mathbf{B_0}$, the effective magnetic field can be written as

$$\boldsymbol{B_{eff}} = \boldsymbol{B_{rot}} + B_0\hat{x} \tag{3.16}$$

However, this gives rise to a time-dependent Hamiltonian. To combat this and use the framework that we have established so far, we reconsider the Schródinger equation, still in the $\hat{\boldsymbol{x}}$ basis. This yields two coupled differential equations

$$i\hbar\frac{dc_+(t)}{dt} = \frac{\hbar\omega_0}{2}c_+(t) + \frac{\hbar\omega_1}{2}e^{-i\omega t}c_-(t) \tag{3.17}$$

$$i\hbar\frac{dc_-(t)}{dt} = \frac{\hbar\omega_1}{2}e^{i\omega t}c_+(t) - \frac{\hbar\omega_0}{2}c_-(t) \tag{3.18}$$

These differential equations are more easily solved when considered in the rotating frame. To do so, we consider the state

$$|\tilde{\psi}(t)\rangle = \alpha_+(t)|+\rangle + \alpha_-(t)|-\rangle \tag{3.19}$$

Where $\alpha_\pm(t) = c_\pm(t)e^{\pm i\omega t}$. The differential equations in equations 3.17 and 3.18 can be written in terms of $\alpha_\pm(t)$ with the new term $\Delta\omega \equiv \omega - \omega_0$.

$$i\hbar\frac{d_+(t)}{dt} = -\frac{\hbar\Delta\omega}{2}\alpha_+(t) + \frac{\hbar\omega_1}{2}\alpha_-(t) \tag{3.20}$$

$$i\hbar\frac{d\alpha_-(t)}{dt} = \frac{\hbar\omega_1}{2}\alpha_+(t) + \frac{\hbar\Delta\omega}{2}\alpha_-(t) \tag{3.21}$$

Solving this equation and revisiting Rabi's formula, the probability of a spin flipping from up to down with an oscillating perturbation field is

$$P_{+\to-} = \frac{\omega_1^2}{(\omega-\omega_0)^2+\omega_1^2}\sin^2\left(\frac{\sqrt{(\omega-\omega_0)^2+\omega_1^2}}{2}\mathrm{t}\right) \tag{3.22}$$

Now it can be seen that when $\omega \approx \omega_0$ that the probability given by Rabi's formula is allowed to reach unity at various times.

3.5 Bloch Equations

The probability given above by Rabi's formula in a rotating frame describes the idealized case of particle spin precession. In the laboratory, the nuclear magnetization is seen to have relaxation times in which the spin returns to the lowest energy state. Additionally, we move to the magnetization, $\boldsymbol{M}$, of the spin ensemble, which can be mathematically treated the same as $\boldsymbol{\mu}$. The Bloch equations are a set of equations describing the sample magnetization as a function of time considering these relaxation times. For a strong magnetic field $B_0\hat{\boldsymbol{x}}$ and weak time-dependent perturbing magnetic field, the three differential equaitons are:

$$\frac{dM_x(t)}{dt} = \gamma(\boldsymbol{M}(t) \times \boldsymbol{B_{eff}}(t))_x - \frac{M_x(t) - M_0}{T_1} \tag{3.23}$$

$$\frac{dM_y(t)}{dt} = \gamma(\boldsymbol{M}(t) \times \boldsymbol{B_{eff}}(t))_y - \frac{M_y(t)}{T_2} \tag{3.24}$$

$$\frac{dM_z(t)}{dt} = \gamma(\boldsymbol{M}(t) \times \boldsymbol{B_{eff}}(t))_z - \frac{M_z(t)}{T_2} \tag{3.25}$$

Notice that as T_1 and T_2 approach infinity, Eqs. 3.23 - 3.25 reduce to the equation of motion of the sample magnetization given by Eq. 3.8. Now, we consider only Eq. 3.23 as the MRFM device will only detect force in the $\hat{\boldsymbol{x}}$ direction. The derivation of the solution to the differential equations is found by setting the derivatives equal to zero to find a steady-state solution. This requires that manipulation of the spins allows for spins to relax thermally, discussed more in the following section. When $T_1 \approx T_2 = \tau$ the magnetization in the $\hat{\boldsymbol{x}}$ direction is given by the relation

$$M_x = M_0 \frac{1 + (\omega - \omega_0)^2\tau^2}{1 + (\gamma^2 B_1^2 + (\omega - \omega_0)^2)\tau^2} \tag{3.26}$$

M_0 is the thermal polarizaiton of the spins that the magnetization decays to. Assuming Maxwell-Boltzmann statistics, the expected value of the ensemble magnetization is proportional to the magnetic field strength, B_0.

3.6 Cyclic Saturation and Driving of Spins

There are many ways that external drives are used to create MRFM signals that can be detected by a mechanical resonator with a lower frequency than the Larmor frequency. Three popular detection schemes are iOscar, adiabatic rapid passage, and cyclic saturation. iOscar applies a fixed microwave tone to the perturbation field source that drives the resonator via magnetic force. Adiabatic rapid passage sweeps the microwave signal frequency around the Larmor frequency at the rate of the mechanical frequency. Cyclic saturation amplitude or frequency modulates the microwave signal in the perturbation field source at the frequency of the mechanics. Cyclic saturation is the simplest detection scheme, but requires short relaxation times of 10 to 100 ns. This is not well suited for the ultimate systems of interest (electron or nuclear spins) that have longer relaxation times and is the reasoning behind the choice of using diphenylpicrylhydrazil (DPPH) with a relaxation time estimated at 62 ns. DPPH also has the property that $T_1 \approx T_2 = \tau$.

More on cyclic saturation and the modulation scheme used will be given in Ch. 5

Chapter 4

Silicon Nitride Membrane Resonators

4.1 Introduction and Theory

MRFM uses mechanical resonators to detects NMR as opposed to pick-up coils. Specifically considered in this work are Si_3N_4membrane resonators that have been studied extensively in the Regal group and have promising parameters suited for MRFM. Previously, [8] demonstrated MRFM with a Si_3N_4membrane resonator. The Regal group aims to take this a step further with engineered membrane resonators. In this chapter, I briefly explore some of the basics of these engineered membrane resonators to motivate their ability to further the detection abilities of MRFM.

These can be treated as damped harmonic oscillators. The equations of motion are then:

$$m_{eff}\frac{d^2x}{dt^2} + m_{eff}\Gamma_m\frac{dx}{dt} + m_{eff}\omega_m^2 x(t) = F_{ext}(t) \tag{4.1}$$

Where Γ_m is the energy damping rate. The equation of motion can be solved in frequency space with the Fourier transform of the displacement [17]

$$x(\omega) = \int_{-\infty}^{\infty} x(t)e^{i\omega t}dt = \chi_m(\omega)F_{ext}(\omega) \tag{4.2}$$

We introduce the mechanical succeptability, $\chi_m(\omega)$ which is given by [17]

$$\chi_m(\omega) = [m_{eff}(\omega_m^2 - \omega^2) - im_{eff}\Gamma_m\omega]^{-1} \tag{4.3}$$

Here we consider the motion of these resonators in the plane of displacement. When no external force is applied to the resonator, there is still this zero-point fluctuations of the amplitude

and random forces due to the thermal energy of the resonator and Brownian motion. while there is nothing particularly quantum about the below descriptions and use of the mechanical resonator, we find the zero- oint length scale to be a convenient unit to discuss sensitivity

$$x_{zpf} = \sqrt{\frac{\hbar}{2m_{\text{eff}}\omega_m}} \tag{4.4}$$

Here, m_{eff} of a given mode, j, and location are given by a weighted mass of the mode shape integrated over the resonator times the physical mass.

$$m_{\text{eff,j}}(x,y) = m_{\text{phys}}\frac{\int_{S_{\text{tot}}} w_j^2(u,v)dudv / \int_{S_{\text{tot}}} dudv}{w_j^2(x,y)}, \tag{4.5}$$

First, we consider the spectral density of position given by a white noise driving force. It is useful for us to consider this representation and not the position representation, as it is useful to consider the spectrum of motion. Considering the Fourier transform of the resonator amplitude as a function of time and frequency written as

$$x(\omega) = \frac{1}{\sqrt{2\pi}}\int_{-\infty}^{\infty} x(t)e^{i\omega t}dt \tag{4.6}$$

In measuring the mechanics, it is often beneficial to consider the measurement of a finite time period, τ. This manifests in the form of

$$\tilde{x}(\omega) = \frac{1}{\sqrt{\tau}}\int_{0}^{\tau} x(t)e^{i\omega t}dt \tag{4.7}$$

This in turn can be used to find the spectral density by the expected value of the square amplitude. In the limit of τ approaching infinity, this converges to the Fourier transform of the auto-correlation function [17].

$$S_{xx}(\omega) = \int_{-\infty}^{+\infty} \langle x(t)x(0)\rangle e^{-i\omega t}dt \tag{4.8}$$

Under quantum mechanical considerations, the power spectral density is given by the fluctuation dissipation theorem, which is further detailed in [24]

$$S_{xx}(\omega) = \frac{2\hbar}{1 - e^{-\hbar\omega/k_B T}} Im(\chi_{xx}(\omega)) \tag{4.9}$$

This power spectral density can be related to the force power spectral density, S_{FF} given the spring constant of the resonator [17].

$$\sqrt{S_{FF}} = \frac{4k_B T k}{\omega_m Q} = \frac{2\hbar k_B T}{Q x_{zpf}^2} \tag{4.10}$$

Therefore, in the pursuit of lower force sensitivity, both a high quality factor and high zero-point fluctuations are desireable. There are two methods in which this can be approached: resonator material and resonator design. In this chapter, the promise of tensioned silicon nitride (Si_3N_4) resonators are explored and advanced mechanical designs are studied.

The reported devices are not the only advanced mechanical resonators applicable for force sensing: other silicon nitride membranes and strings [25, 13, 12, 26, 27, 28, 29, 30, 31, 32], silicon cantilever [33], and nano-wires [34]. The SiN devices range in thickness from 20 to 80 nm and in width and length from hundreds of micrometers to several millimeters. The membranes have achieved a force sensitivity as low as 10 aN/$\sqrt{\text{Hz}}$ at room temperature [25] while string resonators were demonstrated to have a force noise floor of 3 aN/$\sqrt{\text{Hz}}$ [13]. The silicon cantilever resonators were shown to have a force noise floor of ≈10 aN/$\sqrt{\text{Hz}}$[35] while the nanowires of smaller mass were shown to have a force noise floor of 2 aN/$\sqrt{\text{Hz}}$ [34]. Larger devices correlate with better force sensitivities, but the much lower frequencies below 150 kHz [26, 25] do not move towards the 10 MHz frequency needed for resonant coupling with nuclear spins that smaller device tend towards [13, 12].

4.2 Trampoline Resonators

Mechanical resonators come in every shape and every size, from the large kg-scale mirrors at the LIGO observatory to the vibrations of an optically suspended atom [17]. Of particular interest to this experiment is two-dimensional Si_3N_4membrane resonators. Due to low optical absorption and high quality factors, tensioned Si_3N_4strings and drums are ideally suited for optomechanical sensing[36]. As mentioned in the introduction to this section, the desirable trait in a mechanical resonator is a low force noise floor and high frequency. Referring back to Eq. 4.10 we see that to lower our force noise floor, we want to simply increase guality factor and zero-point fluctuations (lower mass). While I say simply, and the equation supports this, the actual process of designing a low mass, high Q resonator is difficult.

Force detection of the magnetization of a sample due to magnetic resonance has been detected with Si_3N_4membrane resonators [8]. In an effort to further reduce the force noise floor, mass is removed from the membrane to form a trampoline resonator [37, 25, 26, 1]. The trampoline design removes large sections of the $Si_3N_4$to reduce the mass. Four tethers from each corner of a square frame suspend a central pad.

4.2.1 Design

Trampoline resonators have been shown to have low force noise floors and have promise as force sensing devices. However, the devices presented in [37, 25, 26] are made in varying sizes. As force sensitivity depends in part on x_{zpf}, a trampoline should have high x_{zpf}in not only the pad, but the tether so that one location can be used for optical probing and the other for magnetic coupling.

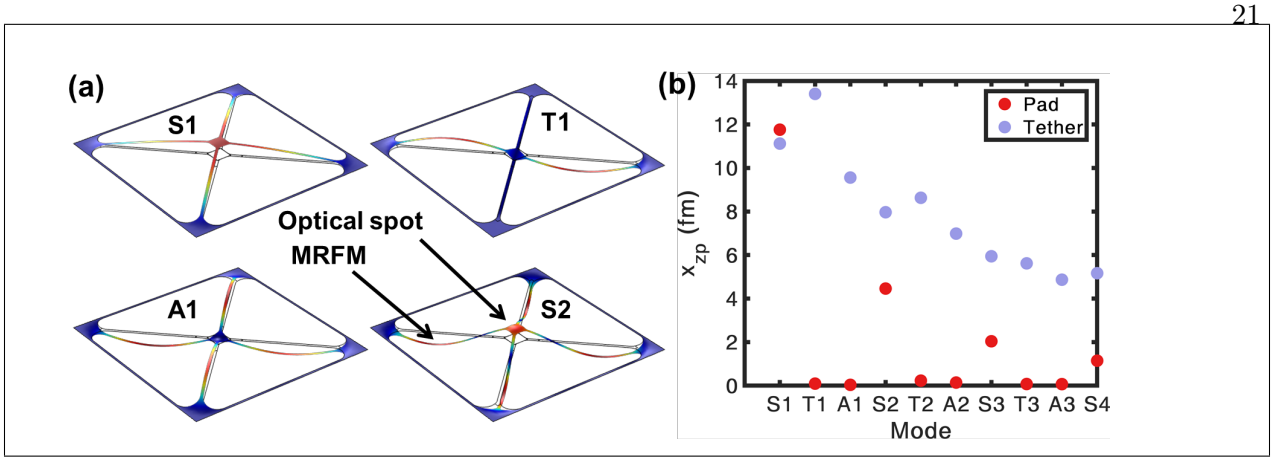

Figure 4.1: Finite element simulation (COMSOL) of a 500 µm wide and 30 nm thick trampoline with a pad size of 30 µm and a tether width of 2 µm. We note S1, T1, A1, S2 as the first symmetric, first torsional, first asymmetric and second symmetric modes, with frequencies of 359 kHz, 912 kHz, 936 kHz and 1140 kHz, respectively. (a) Trampoline mode shapes. Arrows indicate the cavity mode position and the magnetic coupling position, i.e. the position where the magnetic grain or spin sample are deposited on the trampoline. (b) Simulated zero-point fluctuation of the trampoline pad (blue circles) and tether (red circles) for the first trampoline modes, up to S4, ordered from left to right by increasing resonant frequencies. From [1]

The trampoline resonator was modeled with COMSOL Multiphysics and the zero-point fluctuations of the resonator were simulated for various modes, as shown in Fig. 4.1. In particular, we see that in the normal mode (S1) of the trampoline, both the tether and the central pad have high x_{zpf}. This makes the S1 mode of that particular design favorable for coupling action from two locations on the resonator.

4.2.2 Fabrication

Trampoline resonators are fabricated in a multi-step process, shown schematically in Fig. 4.2, and described in detail here. Double-side polished silicon wafers are commercially coated with high-stress stoichiometric silicon nitride (Si_3N_4). The silicon has a crystaline axis defined by $\langle 1\ 0\ 0 \rangle$. The commercial wafers are diced with a saw into 5 mm by 5 mm square chips. The chips undergo a rigorous cleaning, briefly detailed here: one minute rigourous stirring in each of acetone, isopropyl

alcohol, methanol and water; one hour suspended in Nano-strip at a plate temperature of 150°C and gentle stirring; two minutes gentle stirring in each of three clean water baths and an isopropyl alcohol bath; dried with pressurized nitrogen.

The cleaned chips are then coated in a negative UV photoresist, S1813, on both sides, with the following recipe: 1000 rpm for 5 seconds, 4500 rpm for 30 seconds, cure at 115°C for one minute. Then the chip is exposed to UV radiation for 30 seconds with a negative resist to develop a square window. The back window is developed with gentle stirring in 2% TMAH developer for one minute and the rinsed in water. This process is repeated for an e-beam resist to pattern the trampoline resonator in a direct write SEM. After the resist is developed, the same RIE recipe is used. The chip is then cleaned in solvents and put in a 30% KOH bath at 180 °C to release the Si_3N_4. The chips are then gently stirred in water baths and cleaned in Nano-strip as detailed above.

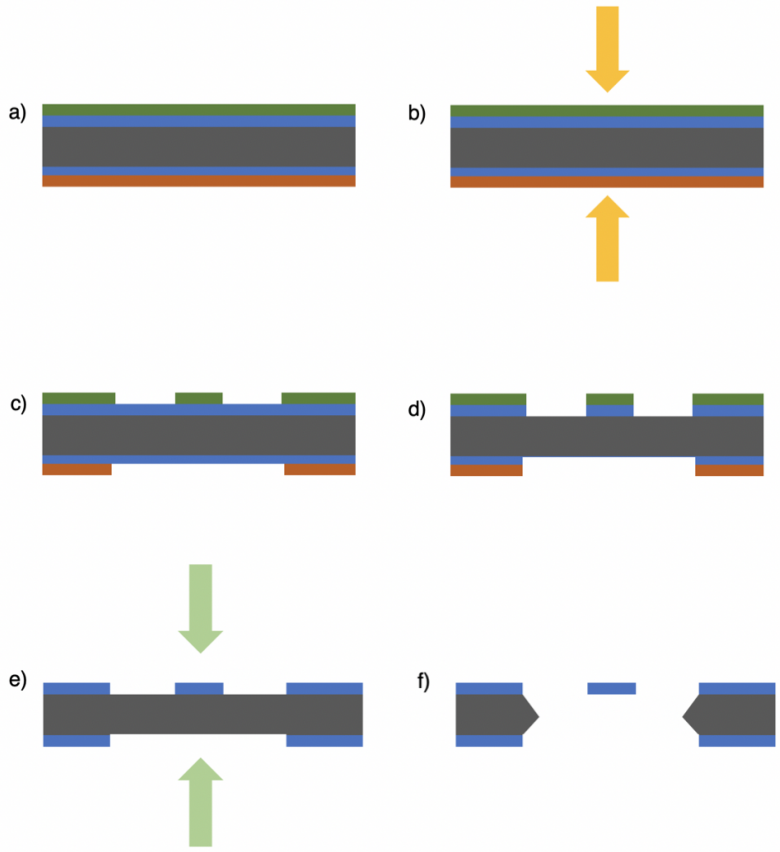

(a) Coat 5 mm square chip with electron beam resist on top, photo-definable resist on the bottom.

(b) Expose resists with desired pattern: resonator profile on top of chip, square window on bottom.

(c) Develop resists.

(d) Dry etch exposed Si_3N_4in reactive ion etcher.

(e) Remove resists and etch exposed silicon with 30% concentration KOH solution from both sides.

(f) Final cross section of fabricated resonator.

Figure 4.2: Cross sections of fabrication steps for 500 μm trampoline. Materials: grey (silicon), blue (Si_3N_4) brown (photoresist), green (electron-beam resist). Exposures: yellow (UV light, electron beam), green (KOH solution).

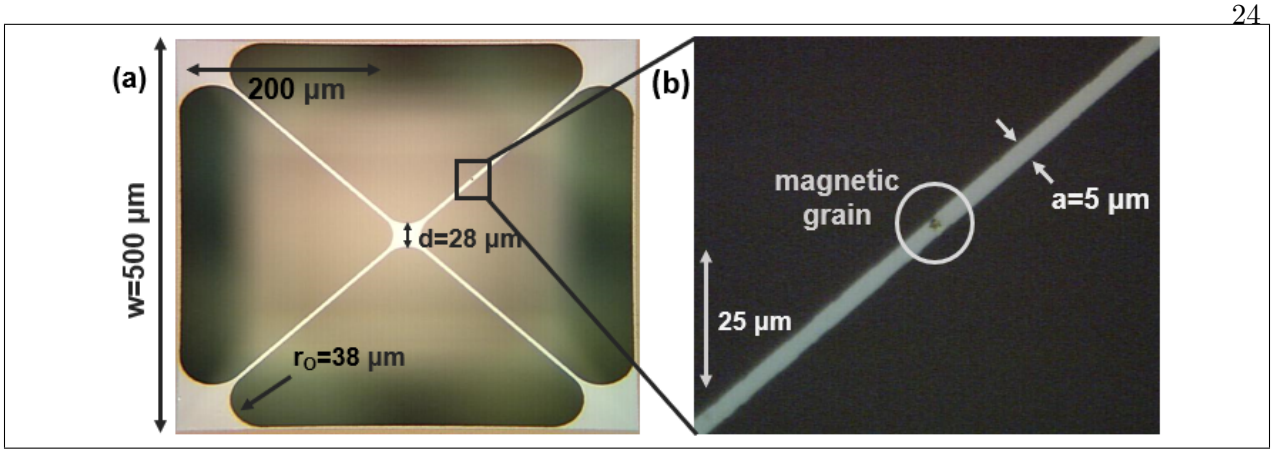

Figure 4.4: (a) SiN Trampoline resonator. (b) Zoom in of functionalized resonator with NdFeB magnetic grain deposited. [1]

4.2.3 Trampoline Characterization

The trampolines are characterized using a Michelson interferometer, which induces two voltages on a balance detector. This is then output to a network analyzer. A network analyzer is used so that a piezo electric transducer (PZT) can drive the mechanics to resonance. The thermal spectrum of the resonator is first analyzed to determine the frequencies of various modes of the resonator. The normal modes of the two trampoline devices studied are reported in table 4.1. Then, the trampoline is driven to resonance by the network analyzer and PZT. The drive is stopped suddenly, and a ringdown measurement is taken. To find the Q of the resonator, an exponential decay is fit to the time trace of the resonance peak. The energy decay time of the resonator, τ_m, is then used to calculate $Q = \omega_m \tau_m$.

4.3 Phononic Crystal Structures

The trampoline resonator is a good force sensor. However, in the pursuit of sub-attonewton force sensitivities, we aim to increase Q further. To approach this goal, we consider Si_3N_4membrane resonators that are patterned with a crystal lattice. This lattice is engineered to have a band gap in spectrum at which the resonator does not have modes. A defect is then introduced in the center of the lattice that perturbs the system and has modes with frequency in the band gap. Following,

Table 4.1: Critical dimensions of each trampolines in devices A and B. t is the SiN thickness, w is window size, r_o is the outer fillet radius, d the central pad length, a is the tether width, and m_{eff} is the calculated resonator's effective mass of the fundamental mode, at the pad position, using Eq. 4.5. Dimensions are depicted in Fig. 4.4. From [1]

Device	A	B
t	30 nm	70 nm
w	500 µm	500 µm
r_o	36 µm	15 µm
d	28 µm	28 µm
a	5 µm	5 µm
m_{eff}	0.5 ng	0.9 ng
f_{S1}	429.1 kHz	389.8 kHz
Q	4.5 $\times 10^6$	1.8 $\times 10^6$
$\sqrt{S_{FF}}$	67 aN/$\sqrt{Hz}$	102 aN/$\sqrt{Hz}$

I discuss how the phononic crystal (PnC) structure allows for increased Q in a Si_3N_4resonator.

There are two main types of loss in a Si_3N_4membrane resonator, here called bending and radiative loss. Bending loss arises from the curvature of the resonator's mode shape. Radiative loss is considered as the acoustic waves moving into the surrounding silicon chip and environment. Since loss mechanisms adds in series, Q adds as in parallel:

$$Q_{tot}^{-1} = Q_{bend}^{-1} + Q_{rad}^{-1} \tag{4.11}$$

The bandgap in the PnC crystal controls the radiative loss. Another effect is called soft clamping and minimizes the bending losses in the resonator, maximizing Q. Current research is exploring the mathematical treatment of values including Q and loss in PnC structures [12, 3]. For simplicity, this thesis will table theoretical models of the resonators and focus on the first successful experimental realization of PnC structures and their parameters.

We studied five principle designs based on two main crystal structures. These five designs are detailed in Fig. 4.5 and briefly summarized here. There are two different PnC structures, one lattice similar to [12] seen in $\triangle$, $\bigcirc$, $\bigtriangledown$ and one lattice that removes more mass seen in + and $\times$ in Fig. 4.5. Each PnC has a characteristic defect shape that resembles the central pad of a trampoline of varying sizes. These are shown in the maps of Fig. 4.5 and described in detail in [3].

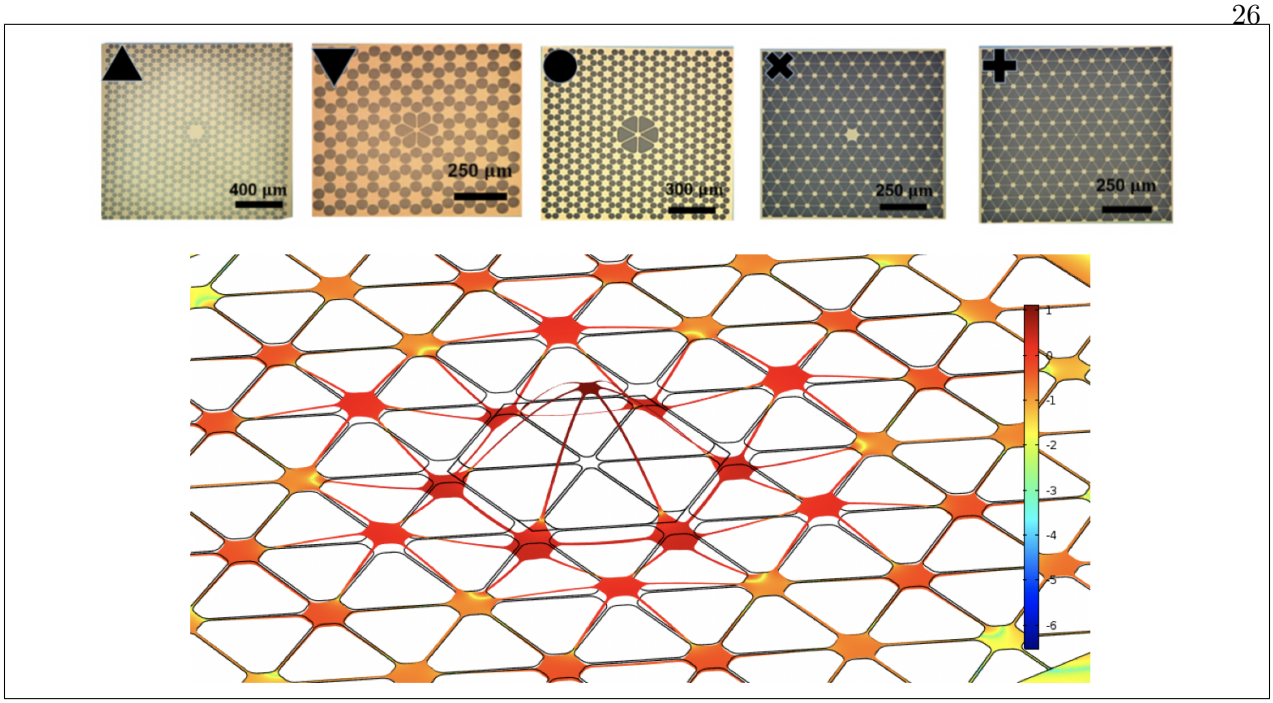

Figure 4.5: The top row shows pictures of devices. [3] Bottom: Localized mode of +, visualizing soft clamping effects.

4.3.1 Fabrication

The PnC resonators were fabricated similarly to the trampoline resonators (Fig. 4.2), with a few changes. The crystal structures were patterned in 100 nm thick LPCVD Si_3N_4on 385 µm silicon. Instead of electron beam and UV-mask photolithography, the resist was patterned with a direct write photolithography system in a grid on the wafer. The $Si_3N_4$was then released using a single-sided etch from the non-resonator side of the wafer in 70 °C KOH for 6 hours. After KOH exposure, the $Si_3N_4$was optically determined to be 85 nm.

Single side etching is necessary with the more complicated geometry of PnC structures relative to trampoline resonators because of the crystallographic axis of ⟨1 0 0⟩ silicon. The single side etch is done by protecting the resonator side of a patterned wafer in a PEEK wafer chuck. In Fig. 4.3f, it is seen that the KOH etches the silicon at an angle, specifically 54.3°. In this manner, KOH does not etch beneath $Si_3N_4$and it etches along the axis of the silicon. During a double-sided etch process, this leaves unetched silicon suspended on the back of the resonator. This added mass

breaks the structure, and is avoided by protecting one side of the wafer during the wet etch process.

4.3.2 Results

PnC structures were measured using an etalon interferometer both at room temperature (10^{-7} mBarr chamber) and 4K (closed cycle cryostat). The resonator is mounted on a mirror on a piezo electric transducer (PZT) to form the etalon. The power spectral density of the signal from the etalon interferometer is analyzed to determine the amplitude and frequency of mechanical modes.

The mechanical spectra of all devices were taken to verify the presence of a band gap and to see the presence of defect modes within the band gap. To capture the full spectrum, each resonator was measured at two locations, one on the defect (orange) and one in the crystal (blue). The locations measured and the mechanical spectra for + and $\triangle$ are shown in Fig. 4.6. Measurements were taken both near the defect and in the crystal structure to illustrate the defect mode locations within the band gap.

It should be noted that Fig. 4.6 shows the measurement location to be on the tether of both the defect and the crystal. This was done to capture modes with frequency above the band gap, as these primarily manifest in tether movement and not in the pads. Quality factors were then taken via ringdown measurements and the same fitting process outlined in Sect. 4.2.3. The fabricated resonators and an example of soft clamping effects are shown in Fig. 4.5. In the plot of out of plane displacement, it is seen that the mode is well isolated to the defect. This verifies that the defect mode is internal loss limited and therefore we can neglect radiative losses [3].

It was observed that at 4 K, all but one device recorded normal mode quality factors above Q $= 10^6$. Given the thickness of the Si_3N_4used compared with other devices [25, 13, 12, 26, 28, 29, 31, 32] that reach down to 20 nm thick, these quality factors are desirable. We estimate that by using 20 nm $Si_3N_4$the quality factor will increase by two orders of magnitude, given that $Q \propto h^{-3}$ [3].

The force sensitivities for all five devices were calculated at both room temperature and at cryogenic temperatures. It was seen that lower x_{zpf}gives a higher force noise floor and less

sensitivity. Moving forward, these devices will be adapted for functionalization and improved quality factors such that they are ideal for cavity optomechanical integration for enhanced spin detection.

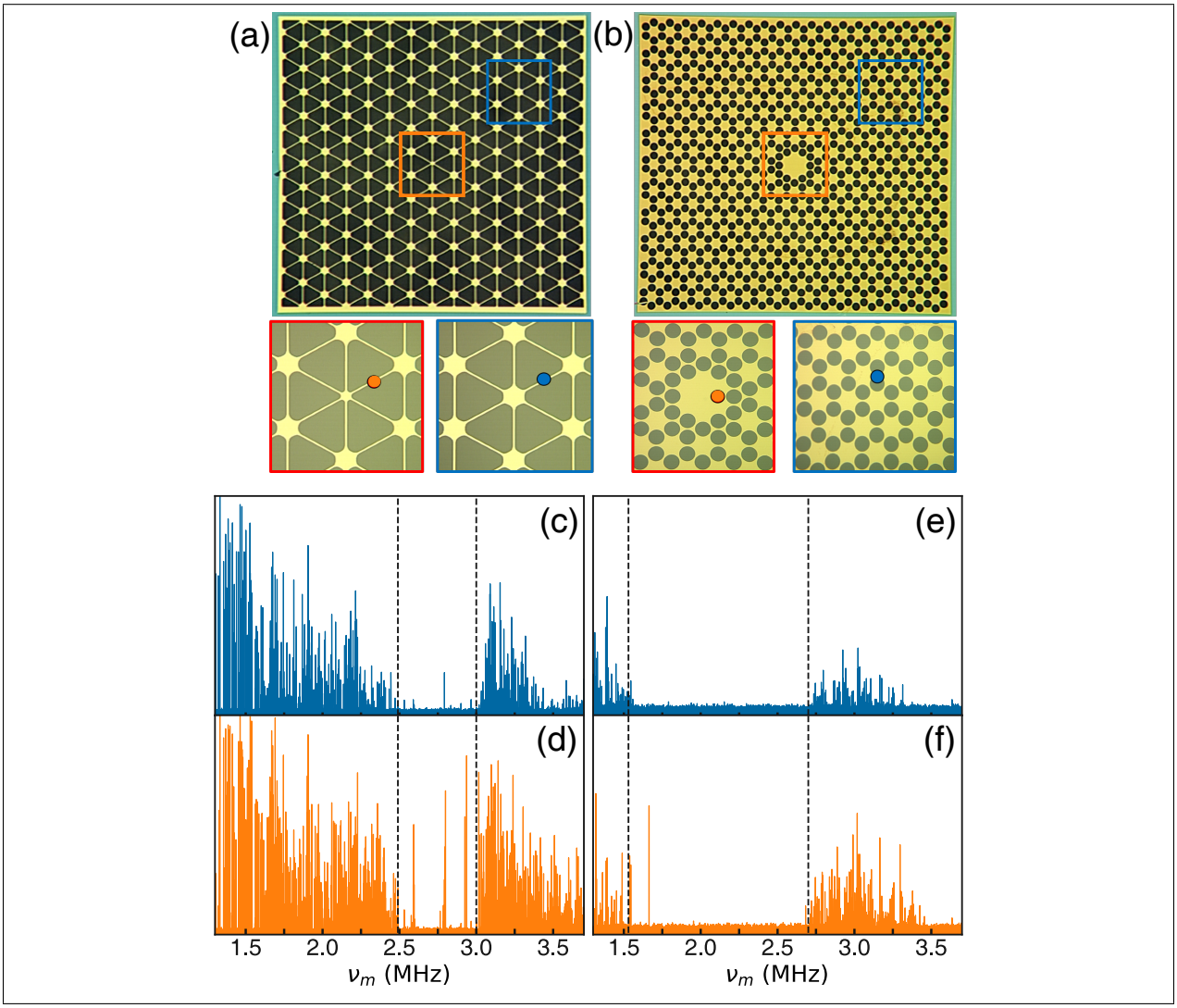

Figure 4.6: (a) Low contrast PnC resonator with (b) High contrast PnC resonator. Dots show location of measurement of spectra.(c-f) Mechanical spectra for the two resonators at the colored locations. [3]

Chapter 5

Magnetic Resonance Force Detection with SiN Membrane Resonators

5.1 Introduction

So far, we have discussed the motivation behind the experiment in Ch. 1. We briefly introduced Optomechanics and related fields in Ch. 2 to frame the context for the experiment. Chapters 3 and 4 give background and context as to how we drive spin and how we measure that resonance. Having covered what we drive, what it couples too, and how we measure that coupling, it is now time to dive into the manifestation of these three components as integrated into a single device. After diving into the geometry and fabrication of the MRFM device, I will present the results of the experiment and the successful detection of electron spins with a micromechanical trampoline resonator. As menitoned in the introduction, this experiment demonstrates a first success at sensing electron spins in DPPH, which provides a large force signal. This allows us in the Regal group to benchmark group capabilities of MRFM detection.

5.2 Device

The MRFM device, referred to as a flip chip consists of three main components: two thin chips that are brought in close proximity and the external magnetic fields that set the energy levels in the Hamiltonian in Eq. 3.3. One of the two chips we have already been introduced to briefly - the trampoline resonator. The second chip hosts the electron spins the drive for the alternating magnetic field, B_1, described in 3.9.

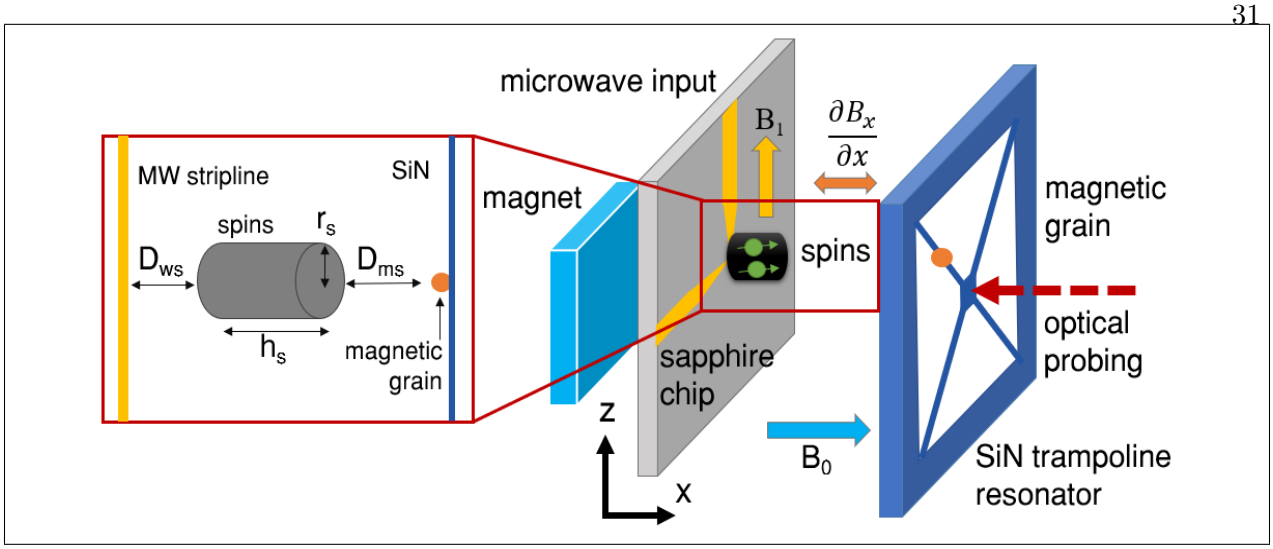

Figure 5.1: Schematic of MRFM experimental device (flip chip).

5.3 Functionalized Trampoline Resonators

The trampoline resonators are functionalized by securing a 3-4 µm diameter grain of NdFeB on one of the tethers with an epoxy glue, 100 µm from the center of the central pad. The deposited magnetic grain is pictured in Fig. 4.4b. One the epoxy cures, the trampoline is put inside a strong electromagnet to induce a permanent magnetization in the grain.

Deposition of the magnetic grain onto the tether of the resonator changes the mechanical properties of the resonator, primarily the quality factor, Q, and the mechanical frequency, Ω_m. Fig. 5.2 depicts the change in both the mode shape and frequency of the first asymmetric mode of the trampoline. Particularly, in Fig. 5.2b, the frequency of the asymmetric mode in which the tether with the grain has greatest displacement (pictured in Fig. 5.2a) is shifted more than the asymmetric mode in which the tether has small amplitude.

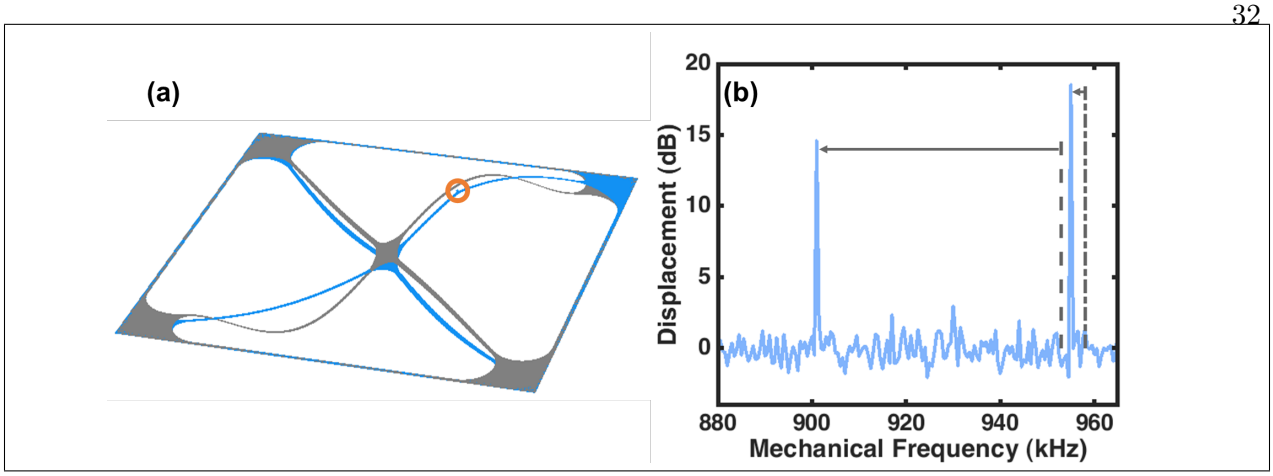

Figure 5.2: Torsional-mode (T1) mode shapes and frequencies prior to (grey) and after (blue) deposition of a magnetic grain. (a) Simulated mode shapes of a free trampoline (grey) and a trampoline deposited with a cubic magnetic grain with an edge size of 2.5 µm(blue). The position of the deposited magnetic grain is marked by a red circle. (b) Measured trampoline displacement spectrum showing resonance location after deposition in blue. The original position of the resonances prior to deposition appear as vertical grey lines. The arrow show the reduction of the mode frequencies after deposition. From [1]

While not pictured in Fig. 5.2, the fundamental mode of the trampoline resonators is impacted to a lesser degree than the asymmetric mode. The frequency is decreases by 10 kHz and the quality factor decreases by a factor of 2, as seen in Table 5.1. The small impact on frequency and quality factor of the magnetic grain deposition maintains the desirable properties outlined in Sect. 4.1.

5.3.1 External Magnetic Fields

The magnetic bias field B_0 is created using a permanent NdFeB commercial magnet. A field of approximately 1 kG along the x-axis is created by the $\frac{1}{2}$" $\times \frac{1}{2}$" $\times \frac{1}{8}$" NdFeB cube. The gyromagnetic ratio, γ, for an electron is 2.8 MHz/G. The bias field is the dominant factor in determining the Larmor frequency at $\omega_0 \approx \gamma B_0$.

Table 5.1: Fundamental mode frequencies and quality factors of the resonators before and after deposition of the NdFeB magnetic grain, calculated spring constant and zero-point fluctuation (derived from the effective mass of Table 4.1) and the corresponding room-temperature force sensitivity, after deposition. From [1]

	Device	A	B
Trampoline	f_{S1}	429.1 kHz	389.8 kHz
	Q	4.5×10^6	1.8×10^6
Trampoline with magnet	f_{S1}	413.2 kHz	379.6 kHz
	Q	2.4×10^6	1.7×10^6
	k	3.4 N/m	5.3 N/m
	x_{zpf}	6.3 fm	4.9 fm
	$\sqrt{S_F}$	67 aN/$\sqrt{\text{Hz}}$	102 aN/$\sqrt{\text{Hz}}$

5.3.2 Microwave Drive

In Secs. 3.3 and 3.4 I discuss the perturbation field (B_1) necessary for magnetic resonance. The desired characteristics include a magnitude smaller than the bias magnetic field and alternating at a frequency close to the Larmor frequency. To deliver this field to the spins, we establish an alternating current across a gold strip line on a sapphire chip.

The strip line pattern is defined with a photodefineable lift-off resist. Then 5 nm of Titanium is evaporated onto the chip, followed by 400 nm of gold. The titanium is included as a bonding agent between the gold and the sapphire substrate. The excess metal and resist is removed with a lift-off solvent. The final strip line is pictured in the inset of Fig. 5.3. In these studies, devices A and B had slightly different gold patterns. In initial designs, the curved elbow at the corner of the strip line was included as a partial cavity to increase signal. However, separation distance was not precise enough and the effect was diminishing. It was observed that the signal in device B was lower than expected. For device A, the curved elbow reflector was removed and replaced with a through-hole in the sapphire chip. The bottom chip was modified for two reasons. First, as mentioned in Ch. 2, tensioned Si_3N_4resonators are aptly fit for cavity optomechanics integration. Benefits of cavity optomechanical integration include damping of mechanics, the benefits of which are discussed in Ch. 2.

Then, an approximately 12 µm radius cylindrical grain of DPPH is placed at the elbow of

the strip line, seen in the inset to Fig. 5.3. The DPPH is secured in epoxy resin. This epoxy gives a separation distance in x such that the spins are not immediately touching the strip line. This separation distance, D_{ws}, is seen in the inset of Fig. 5.1. This distance is critical to estimating the magnitude of B_1, which is fit to experimental data.

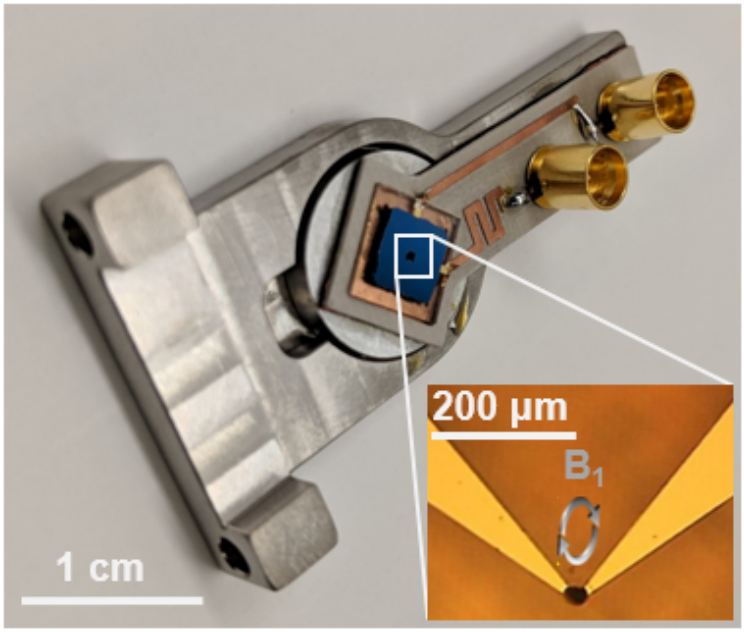

Figure 5.3: Image of final flip chip. Inset: Bottom chip with Au microwave strip line and deposited DPPH grain.

5.3.3 Flip Chip Assembly

The final assembly is achieved by bringing the two chips in close proximity to each other. The functionalized trampoline resonator is "flipped" over so that the magnetic grain can be brought to approximately $D_{ms} = 10\,\mu\text{m}$ from the top of the DPPH spins as seen in the inset of Fig. 5.1. The resonator is aligned so that the magnetic grain is directly over the DPPH grain. The separation is fixed with stycast epoxy on three corners of the chip. Finally, the flip chip is placed in front of the permanent magnet described in Sect. 5.3.1 at a distance such that the magntiude of the field is approximately 1 kG.

5.4 Experiment and Results

There are two MRFM detection schemes that we use in the context of cyclic saturation - amplitude and frequency modulation of the perturbation field. Each of these schemes are carried out either by setting the Larmor frequency of the spins and sweeping the perturbation field frequency from $\omega \ll \omega_0$ to $\omega \gg \omega_0$ or by setting the perturbation field frequency and sweeping the magnetic field that sets the Larmor frequency of the spins. Here, I report results from three of the four possible experimental configurations.

5.4.1 Amplitude Modulation Detection

The perturbation field described in Eq. 3.15 is amplitude modulated at the mechanical frequency, $\omega_m/2\pi$. As the perturbation field is amplitude modulated at the mechanical frequency, the field is turned on and off such that the magnetization oscillates between M_0 and $M_0 - \delta M_x$ given by the minimum of Eq. 3.26. Since this modulation is done at the mechanical frequency, M_x must reach steady state quickly. This is why the relaxation time must be short compared to the time scale of $2\pi/\omega_m$ [33]. The force from the oscillations in the presence of a magnetic field gradient G is described primarily by the first harmonic Fourier component of the magnetization and given by the integral over the volume of the spins [33]:

$$F = \frac{2}{\pi} \int \frac{M_0 \gamma^2 B_1^2 \tau^2}{1 + [\gamma B_0(x) - \omega]^2 \tau^2 + \gamma^2 B_1^2 \tau^2} G A(x) dx \tag{5.1}$$

Here $A(x)$ is the cross-sectional area of the spin sample.

The AM drive was swept over the resonant frequency and the motion of the normal mode recorded as seen in the spectra in Fig. 5.4 for device B. It is noted that as the magnitude of B_1 is increased, there are substantial sources of noise due to spurious electrical forces [1].

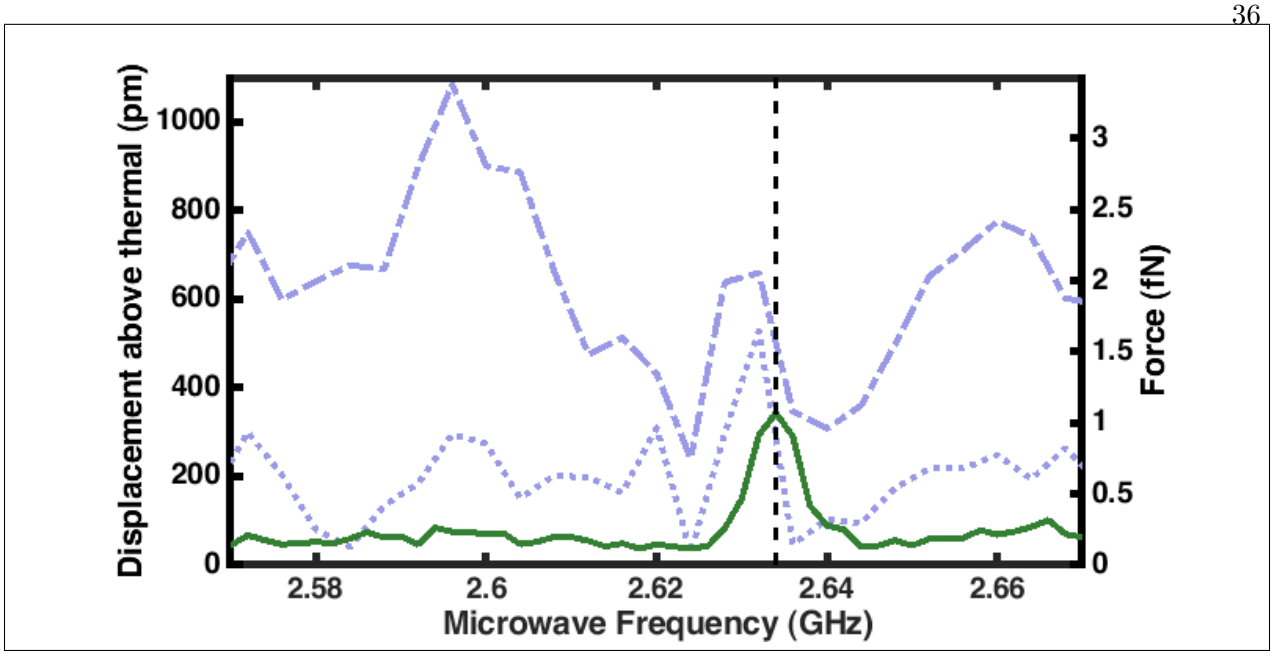

Figure 5.4: MRFM resonance using an AM microwave drive of device B. We show a sweep of the MW frequency at a fixed magnetic field at three different MW powers of -8 dBm (full green), -3 dBm (dotted blue), and 0 dBm (dashed blue). Particularly using the AM technique, the spin-resonance signal can easily be overwhelmed by spurious electrical forces, as observed at the higher powers (dotted blue, dashed blue). [1]

5.4.2 Frequency Modulation Detection

Frequency moculation (FM) cyclic saturation is done by varying the frequency by a small amount (Ω) at the mechanical frequency. Similarly to AM detection, the first harmonic Fourier component is dominant in the magnetizaiton of the sample and therefore the force. This is given by the derivative of Eq. 3.26 in frequency space [33]. The force as a function of frequency is then given by:

$$F = \int_0^\infty \Omega M_0 \frac{\partial}{\partial \omega} \Big[\frac{\gamma^2 B_1^2 \tau^2}{1 + (\gamma[B_0(0) + Gx] - \omega)^2 \tau^2 + \gamma^2 B_1^2 \tau^2} \Big]_{\omega = _0(0)} GAdx \tag{5.2}$$

Device A was measured using FM cyclic saturation, with spectra given in Fig. 5.5 in units of force. Additionally plotted in Fig. 5.5 is a fit to the measured force and the adjusted phase shift that was not directly measured.

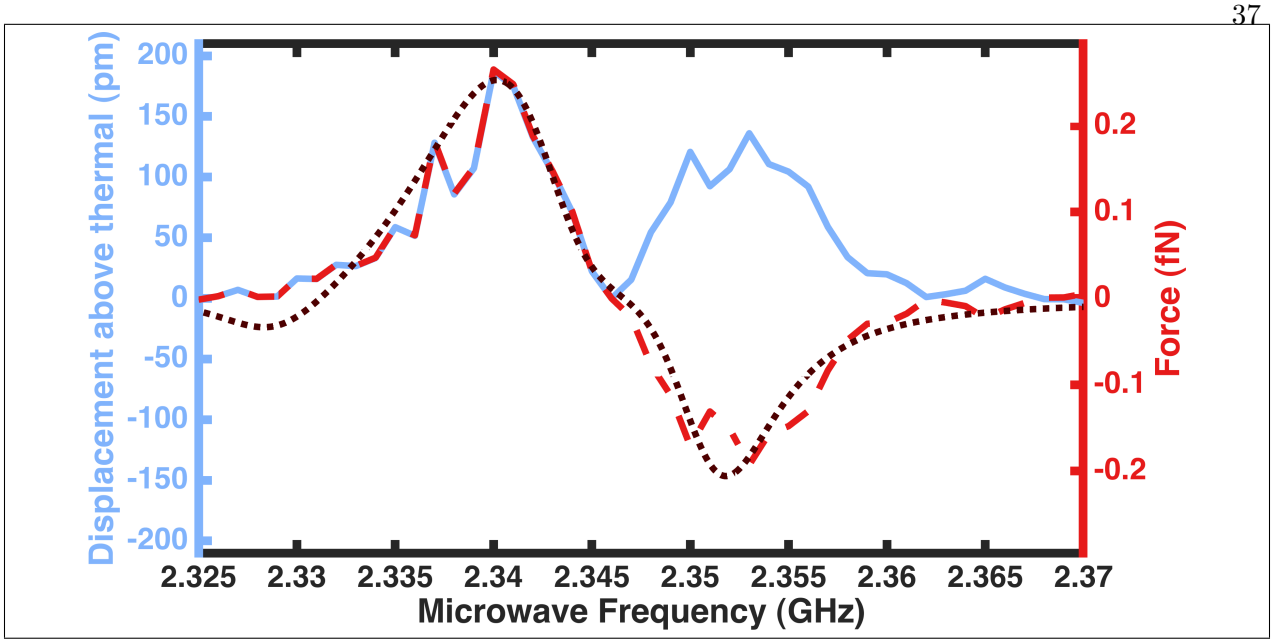

Figure 5.5: MRFM resonance from device A using an FM microwave drive. The MW frequency is swept at a fixed magnetic field. Shown are the mechanical displacement (full blue), the corresponding force signal (dashed red), and a fit of the FM signal (dotted black). The input microwave drive power is -7 dBm. From [1]

The values used in the fit are given in table 4.1 and the dimensions are illustrated in the inset of Fig. 5.1. These agree to within fabrication uncertainties to the geometries of the flip chip.

5.4.3 Varying Larmor Frequency

The two data sets given use the method of sweeping over the microwave frequency to capture the resonance and determine the Larmor frequency. As mentioned above, the resonance can also be detected by sweeping the Larmor frequency and holding the microwave frequency constant. This is done with the introduction of an additional permanent magnet. A micrometer feed through was added to the chamber that was able to position the additional magnet along the x-axis relative to the flip chip pictured in Fig. 5.6.

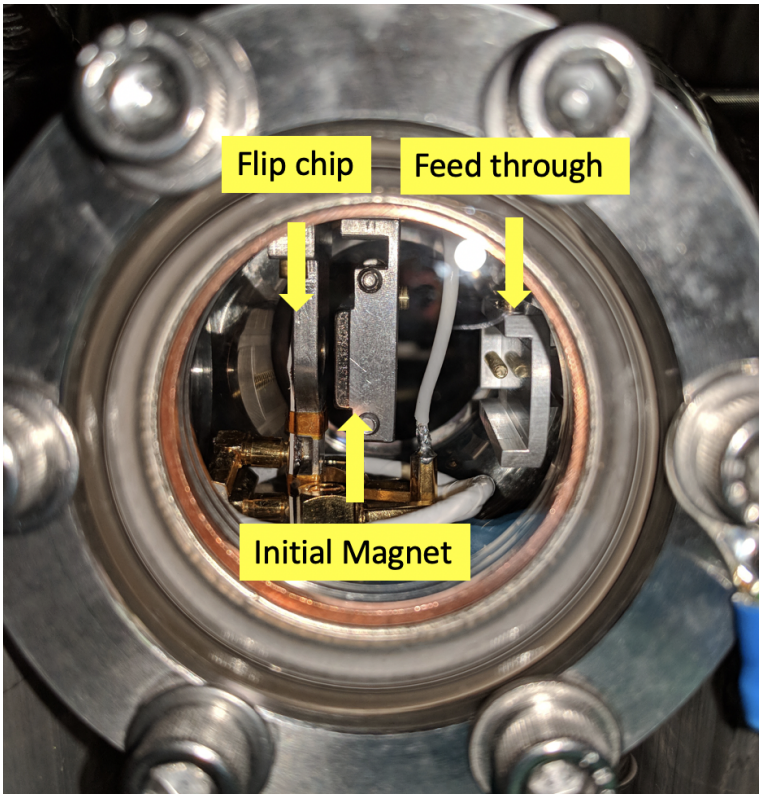

Figure 5.6: Image of the magnetic feed-through for varying the Larmor frequency at the location of the spins in relation to the location to the experimental set up.

The secondary magnet was positioned at least 1 cm from the flip chip to the the contribution to the magnetic gradient was minimal and greater precision in magnetic field could be obtained. The gradient was on the order of 10 G/mm for the entire sweep which is small compared to the $\approx$ 200 G/mm gradient from the primary magnet. The results of the sweep are plotted in Fig. 5.7 along with the fit and phase shift accommodation, as in Fig. 5.5.

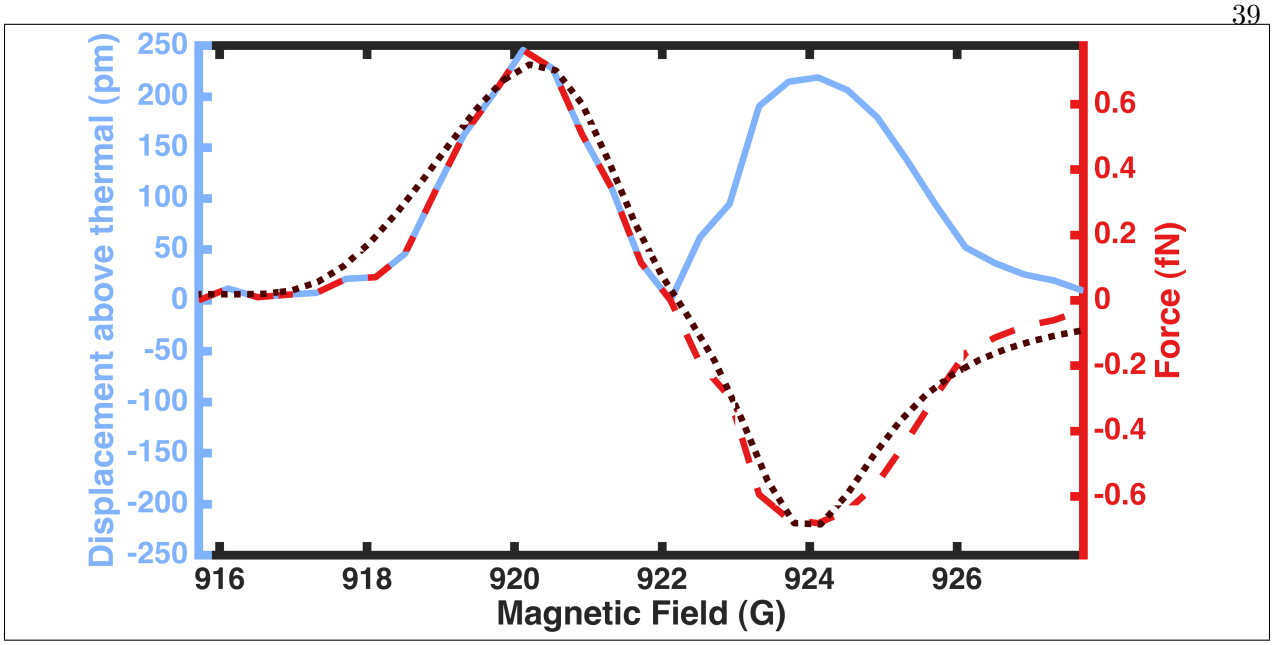

Figure 5.7: Same as Fig. 5.5, but here we sweep the magnetic field at a fixed microwave frequency of 2.564 GHz and use device B. The input microwave drive power is -7 dBm. From [1]

The values used in the fit are given in table 4.1 and the dimensions are illustrated in the inset of Fig. 5.1. These agree to within fabrication uncertainties to the geometries of the flip chip.

Chapter 6

Conclusion

In this work, I present the successful realization of an experiment to detect electron spins in DPPH via MRFM techniques. Specifically, patterned Si_3N_4membrane resonators were utilized to both push force sensitivity lower and provide the opportunity for future cavity optomechanical integration. This experiment used a trampoline resonator to couple magnetic interactions between a magnetic grain and driven electron spins to the optomechanical interactions of light incident on a mechanical resonator. By using the cyclic saturation MRFM detection scheme, we measure both AM and FM signals with force noise floors as low as 67 $aN/\sqrt{Hz}$. Additionally, there is clear path forward for the demonstration of < 1 $aN/\sqrt{Hz}$ force sensitivities with the integration and funtionalization of Si_3N_4PnC resonators.

Bibliography

[1] R. Fischer, D. P. McNally, C. Reetz, G. G. T. Assumpcao, T. R. Knief, Y. Lin, and C. A. Regal, "Spin detection with a micromechanical trampoline:Towards magnetic resonance microscopy harnessing cavity optomechanics," arXiv:1811.05718 [cond-mat], Nov. 2018. arXiv: 1811.05718.

[2] D. McIntyre, C. Manogue, and J. Tate, Quantum Mechanics. Pearson, 2016.

[3] C. Reetz, R. Fischer, G. T. Assumpcao, D. P. McNally, P. S. Burns, and C. A. Regal, "In preparation," 2019.

[4] A. O. Sushkov, I. Lovchinsky, N. Chisholm, R. L. Walsworth, H. Park, and M. D. Lukin, "Magnetic resonance detection of individual proton spins using quantum reporters," Phys. Rev. Lett., vol. 113, p. 197601, Nov 2014.

[5] A. Ajoy, U. Bissbort, M. D. Lukin, R. L. Walsworth, and P. Cappellaro, "Atomic-scale nuclear spin imaging using quantum-assisted sensors in diamond," Phys. Rev. X, vol. 5, p. 011001, Jan 2015.

[6] I. Lovchinsky, A. O. Sushkov, E. Urbach, N. P. de Leon, S. Choi, K. De Greve, R. Evans, R. Gertner, E. Bersin, C. Müller, L. McGuinness, F. Jelezko, R. L. Walsworth, H. Park, and M. D. Lukin, "Nuclear magnetic resonance detection and spectroscopy of single proteins using quantum logic," Science, vol. 351, no. 6275, pp. 836–841, 2016.

[7] D. Rugar, R. Budakian, H. Mamin, and B. Chui, "Single spin detection by magnetic resonance force microscopy," Nature, vol. 430, no. 6997, pp. 329–332, 2004.

[8] N. Scozzaro, W. Ruchotzke, A. Belding, J. Cardellino, E. C. Blomberg, B. A. McCullian, V. P. Bhallamudi, D. V. Pelekhov, and P. C. Hammel, "Magnetic resonance force detection using a membrane resonator," Journal of Magnetic Resonance, vol. 271, pp. 15 – 20, 2016.

[9] C. Degen, M. Poggio, H. Mamin, C. Rettner, and D. Rugar, "Nanoscale magnetic resonance imaging," Proceedings of the National Academy of Sciences, vol. 106, no. 5, pp. 1313–1317, 2009.

[10] W. Rose, H. Haas, A. Q. Chen, N. Jeon, L. J. Lauhon, D. G. Cory, and R. Budakian, "High-resolution nanoscale solid-state nuclear magnetic resonance spectroscopy," Phys. Rev. X, vol. 8, p. 011030, Feb 2018.

[11] P.-L. Yu, K. Cicak, N. Kampel, Y. Tsaturyan, T. Purdy, R. Simmonds, and C. Regal, "A phononic bandgap shield for high-q membrane microresonators," Appl. Phys. Lett., vol. 104, no. 2, p. 023510, 2014.

[12] Y. Tsaturyan, A. Barg, E. S. Polzik, and A. Schliesser, "Ultracoherent nanomechanical resonators via soft clamping and dissipation dilution," Nature Nanotech., vol. 12, no. 8, p. 776, 2017.

[13] A. H. Ghadimi, S. A. Fedorov, N. J. Engelsen, M. J. Bereyhi, R. Schilling, D. J. Wilson, and T. J. Kippenberg, "Elastic strain engineering for ultralow mechanical dissipation," Science, 2018.

[14] M. Yuan, M. A. Cohen, and G. A. Steele, "Silicon nitride membrane resonators at millikelvin temperatures with quality factors exceeding 108," Appl. Phys. Lett., vol. 107, no. 26, p. 263501, 2015.

[15] A. Ashkin, "Trapping of Atoms by Resonance Radiation Pressure," Physical Review Letters, vol. 40, pp. 729–732, Mar. 1978.

[16] F. Marquardt and S. M. Girvin, "Optomechanics," Physics, vol. 2, p. 40, May 2009.

[17] M. Aspelmeyer, T. J. Kippenberg, and F. Marquardt, "Cavity optomechanics," Rev. Mod. Phys., vol. 86, pp. 1391–1452, Dec. 2014.

[18] T. Corbitt, Y. Chen, E. Innerhofer, H. Müller-Ebhardt, D. Ottaway, H. Rehbein, D. Sigg, S. Whitcomb, C. Wipf, and N. Mavalvala, "An All-Optical Trap for a Gram-Scale Mirror," Phys. Rev. Lett., vol. 98, p. 150802, Apr. 2007.

[19] S. Gigan, H. R. Bhm, M. Paternostro, F. Blaser, G. Langer, J. B. Hertzberg, K. C. Schwab, D. Buerle, M. Aspelmeyer, and A. Zeilinger, "Self-cooling of a micromirror by radiation pressure," Nature, vol. 444, no. 7115, pp. 67–70, 2006.

[20] O. Arcizet, P.-F. Cohadon, T. Briant, M. Pinard, and A. Heidmann, "Radiation-pressure cooling and optomechanical instability of a micromirror," Nature, vol. 444, pp. 71–74, 2006.

[21] A. Schliesser, R. R, G. Anetsberger, O. Arcizet, and T. J. Kippenberg, "Resolved-sideband cooling of a micromechanical oscillator," Nature Physics, vol. 4, pp. 415–419, Apr. 2008.

[22] J. Thompson, B. Zwickl, A. Jayich, F. Marquardt, S. Girvin, and J. Harris, "Strong dispersive coupling of a high-finesse cavity to a micromechanical membrane," Nature, vol. 452, no. 7183, pp. 72–75, 2008.

[23] R. W. Peterson, Quantum measurement backaction and upconverting microwave signals with mechanical resonators. PhD thesis, University of Colorado, 2017.

[24] U. M. B. Marconi, A. Puglisi, L. Rondoni, and A. Vulpiani, "Fluctuationdissipation: Response theory in statistical physics," Physics Reports, vol. 461, pp. 111–195, June 2008.

[25] R. A. Norte, J. P. Moura, and S. Gröblacher, "Mechanical Resonators for Quantum Optomechanics Experiments at Room Temperature," Phys. Rev. Lett., vol. 116, p. 147202, Apr. 2016.

[26] C. Reinhardt, T. Müller, A. Bourassa, and J. C. Sankey, "Ultralow-Noise SiN Trampoline Resonators for Sensing and Optomechanics," Phys. Rev. X, vol. 6, p. 021001, Apr. 2016.

[27] T. P. Purdy, R. W. Peterson, and C. A. Regal, "Observation of Radiation Pressure Shot Noise on a Macroscopic Object," Science, vol. 339, no. 6121, pp. 801–804, 2013.

[28] R. Schilling, H. Schütz, A. H. Ghadimi, V. Sudhir, D. J. Wilson, and T. J. Kippenberg, "Near-field integration of a sin nanobeam and a sio_2 microcavity for heisenberg-limited displacement sensing," Phys. Rev. Applied, vol. 5, p. 054019, May 2016.

[29] M. J. Bereyhi, A. Beccari, S. A. Fedorov, A. H. Ghadimi, R. Schilling, D. J. Wilson, N. J. Engelsen, and T. J. Kippenberg, "Clamp-tapering increases the quality factor of stressed nanobeams," arXiv:1810.00414 [cond-mat, physics:physics], Sept. 2018. arXiv: 1810.00414.

[30] B. W. Chui, Y. Hishinuma, R. Budakian, H. J. Mamin, T. W. Kenny, and D. Rugar, "Mass-loaded cantilevers with suppressed higher-order modes for magnetic resonance force microscopy," in TRANSDUCERS '03. 12th International Conference on Solid-State Sensors, Actuators and Microsystems. Digest of Technical Papers (Cat. No.03TH8664), vol. 2, pp. 1120–1123, June 2003.

[31] M. Rossi, D. Mason, J. Chen, Y. Tsaturyan, and A. Schliesser, "Measurement-based quantum control of mechanical motion," arXiv preprint arXiv:1805.05087, 2018.

[32] A. G. Krause, T. D. Blasius, and O. Painter, "Optical read out and feedback cooling of a nanostring optomechanical cavity," arXiv:1506.01249, June 2015. arXiv: 1506.01249.

[33] K. Wago, O. Züger, J. Wegener, R. Kendrick, C. S. Yannoni, and D. Rugar, "Magnetic resonance force detection and spectroscopy of electron spins in phosphorus-doped silicon," Review of Scientific Instruments, vol. 68, no. 4, pp. 1823–1826, 1997.

[34] J. M. Nichol, E. R. Hemesath, L. J. Lauhon, and R. Budakian, "Nanomechanical detection of nuclear magnetic resonance using a silicon nanowire oscillator," Phys. Rev. B, vol. 85, no. 5, p. 054414, 2012.

[35] H. J. Mamin and D. Rugar, "Sub-attonewton force detection at millikelvin temperatures," Appl. Phys. Lett., vol. 79, no. 20, pp. 3358–3360, 2001.

[36] Q. P. Unterreithmeier, T. Faust, and J. P. Kotthaus, "Damping of nanomechanical resonators," Phys. Rev. Lett., vol. 105, no. 2, p. 027205, 2010.

[37] D. Kleckner, B. Pepper, E. Jeffrey, P. Sonin, S. M. Thon, and D. Bouwmeester, "Optomechanical trampoline resonators," Optics express, vol. 19, no. 20, pp. 19708–19716, 2011.